Title

Unraveling the Kinetics of Hydride Formation and Decomposition at Pd-Au Bimetallic Interfaces: A Combined Spectroscopic and Computational Study.

Authors

Routh, Prahlad K
Liu, Xihan
Redekop, Evgeniy
et al.

Publication Date

2025-03-01

DOI

10.1021/jacs.5c00842

Unraveling the Kinetics of Hydride Formation and Decomposition at Pd-Au Bimetallic Interfaces: A Combined Spectroscopic and Computational Study

Prahlad K. Routh[1#], Xihan Liu[2#], Evgeniy Redekop[3#], Jin Soo Lim[2], Sebastian Prodinger[3], Jessi E. S. van der Hoeven[4], Joanna Aizenberg[5,6], Maarten Nachtegaal[7,8,9], Adam H. Clark[7], Philippe Sautet[2,10], Anatoly I. Frenkel[1,11*]*

[1]Department of Materials Science and Chemical Engineering, Stony Brook University, Stony Brook, NY 11794, United States

[2]Department of Chemical and Biomolecular Engineering, University of California, Los Angeles, Los Angeles, CA 90095, United States

[3]Centre for Materials Science and Nanotechnology (SMN), Department of Chemistry, University of Oslo, N-0315 Oslo, Norway

[4]Materials Chemistry and Catalysis, Debye Institute for Nanomaterials Science, Utrecht University, 3584 CG Utrecht, The Netherlands

[5]Harvard John A. Paulson School of Engineering and Applied Sciences, Harvard University, Cambridge, MA 02138, United States

[6]Department of Chemistry and Chemical Biology, Harvard University, Cambridge, MA 02138, United States

[7]Center for Photon Science, PSI, Villigen, CH-5232, Switzerland

[8]Center for Energy and Environmental Sciences, PSI, Villigen, CH-5232, Switzerland

[9]Department of Chemistry, ETH Zürich, CH-8093, Zürich, Switzerland

[10]Department of Chemistry and Biochemistry, University of California, Los Angeles, Los Angeles, CA 90095, United States

[11]Division of Chemistry, Brookhaven National Laboratory, Upton, NY 11973, USA

#These authors contributed equally

*Corresponding authors: sautet@ucla.edu, anatoly.frenkel@stonybrook.edu

Abstract

Supported Pd-Au bimetallic nanoparticles are a promising class of catalysts used for hydrogenation and oxidation reactions. Recently, the role of dynamic restructuring of Pd regions at and near the nanoparticle surface in response to modulating gas (H_2 and O_2) concentration was highlighted for controlling the surface Pd oxide stoichiometry. Here we investigate the mechanism of formation and decomposition of Pd hydride (PdH_x) at and near the bimetallic nanoparticle surfaces, a key species for controlling the activity, selectivity and stability of Pd catalysts in many hydrogenation reactions. We employ modulation excitation X-ray absorption spectroscopy (ME-XAS) to directly observe the time-scale of PdH_x formation and decomposition on the surface of Pd-Au nanoparticles. Density functional theory (DFT) calculations provide additional insights into the stability and energetics of PdH_x formation under varying H fractions and Pd sub-structures. Our results reveal a complex interplay between Pd ensemble size, surface structure, and hydrogen environment in determining the kinetics and thermodynamics of PdH_x formation. By elucidating the mechanisms underlying surface PdH_x formation and decomposition, rational design of dynamic catalysts with controlled Pd hydride stoichiometries can become possible.

1. Introduction

Supported palladium (Pd) and its alloy nanoparticles are widely used for catalysis, hydrogen separation, purification, and storage[1]. Recent studies have shown that the structure of the nearest environment of Pd atoms in different surface facets plays a key role in developing low-cost hydrogen carriers for practical fuel cell applications.[2] Pd ensemble sizes define the feasibility of H_2 activation and subsequent hydrogenation and dehydrogenation reactions. Hence, an optimal palladium structure ranging from atomically dispersed to sub-nm and larger Pd clusters is often needed for favorable adsorption and subsequent reactions.[3] In heterogeneous catalysis, Pd-based nanocatalysts catalyze selective hydrogenation of alkynes for large-scale industrial applications.[4] The addition of a second metal, thereby forming alloys, enables a strategy to leverage geometric and electronic effects between the host metal and active catalytic centers to further improve selectivity and activity.[5, 6] Recent efforts have also shown that the catalytic activity of bimetallic alloys can be tuned dynamically by pretreatment of Pd-Au catalysts which results in changes in elemental distribution, ensemble size, and electronic structure at the surface and can possibly enable metastable configurations that deviate from the thermodynamically most favorable configurations.[7-10]

Metallic Pd has a relatively high capacity to dissolve O, C, and H atoms and, depending on the gas environment tends to form oxide, carbide, and hydride phases that may participate in the catalytic reactions. In particular, in hydrogenation reactions, the formation of Pd hydride (PdH_x) is hypothesized to play a role in determining the reaction activity and selectivity.[11-14] Palladium hydride (PdH_x) has been shown to exhibit a phase transition between a low-H content $\alpha-$phase and high-H content $\beta-$phase, and more recently a metastable hexagonal close-packed (hcp) structure at high H content in nanoscale particles has also been evidenced.[15] Pd hydride has been shown to be important for catalyzing hydrogenation reactions[16, 17] and separation science with its application to membranes.[18, 19] The H atoms in PdH_x can be located on the surface, subsurface, and interstitial sites after absorption and dissociation of H_2 on the surface of a Pd cluster or nanoparticle. Thermodynamic stability data[20] and in-situ experimental observation of PdH_x in pure Pd nanoparticles (Pd NPs) have shown that H atoms introduce lattice distortions and the stability of PdHx is dependent on Pd nanoparticle size.[21] The kinetics of

formation of PdH_x in pure Pd and its bulk alloys is well established,[22] but little is known about the kinetics of hydride formation in bimetallic Pd nanoalloys. This is largely due to the difficulty of characterizing sub-nanometric Pd domains and possible inhomogeneous Pd distribution in the alloy within larger bimetallic NPs with standard structural characterization methods such as XRD, XPS, and XAS. Pd and Au are highly miscible but the intra-particle compositional and structural configuration can range from Au-core-Pd-shell[23, 24] to Pd-core-Au-shell[25] structures in addition to quasi-homogenous mixing[26, 27]. The surface distribution of Pd atoms in Pd-Au particles significantly influences the performance of the catalysts, e.g. isolated Pd sites are useful for CO oxidation[28] and higher H_2O_2 selectivity in H_2O_2 synthesis[29] and Pd regions have been shown to have low energy barriers for the oxygen reduction reaction (ORR)[30].

The direct observation of the dynamic surface structures at the sub-nanometer level is experimentally challenging and intermediate catalyst states are often not detected during steady state experimental measurements. The heterogeneity of surface species remains a major research challenge.[31] Modulation excitation (ME) experiments, where the gas environment, temperature, or electric potential are periodically changed, have been shown to enhance signal-to-noise ratio towards the detection of the surface species that actively participate in the (reversible) interaction. ME coupled with X-ray absorption spectroscopy (ME-XAS) also enables probing of intermediate states formed reversibly, present at low concentration. In a recent work, we applied the ME-XAS approach to probe the dynamic restructuring of surface PdO_x, Pd and Pd-Au species in bimetallic (Pd-in-Au) nanoparticles under modulating (H_2 and O_2) gas conditions.[32]

Herein, we examine the role of surface and sub-surface Pd clusters on the dynamics of Pd hydride formation and decomposition, using the previously studied system of ca. 30 atomic % Pd-Au bimetallic nanoparticles (7.7 nm in diameter, with the standard deviation of 2.4 nm[32]) embedded on a SiO_2 support (using a raspberry colloid templated (RCT) synthesis method).[32] The raspberry colloid synthesis approach is a multi-step colloidal synthesis procedure for obtaining well-defined catalysts consisting of a macroporous metal oxide support (in this case silica) with metallic nanoparticles (here: Pd-Au) residing at the pore walls.[32-34] A key feature of the system is that the nanoparticles are substantially

embedded in the support, giving them high thermal stability and making the nanoparticles resistant to sintering at elevated temperatures and under catalytic conditions.

This Pd-Au system has been shown to possess a heterogeneous distribution of Pd atoms within the Au host, ranging from three-dimensional Pd-rich regions[32] to surface Pd_nAu (n = 1, 2, or 3) ensembles.[7] To capture the surface dynamics of the Pd-Au bimetallic nanoparticles we designed an in-situ approach and used periodic modulation of the gas environment between H_2 and He and quantified the local structure of Pd atoms in $Pd_{30}Au_{70}/SiO_2$ and Pd_{100}/SiO_2 nanoparticles by XAS using a fast acquisition rate of 1 Hz. For gas modulation, we used a total of 60 cycles, each cycle consisting of 60 s of He and 60 s of 20% H_2 balanced with He. We hypothesize that periodic switching of gas pulses of He and H_2 will cause the periodic switching of the compositions of Pd regions, from metallic Pd to Pd hydride and back (Fig. 1). This method enabled the observation of near-surface Pd hydride formation and decomposition time scales and estimate the fraction of Pd atoms at and near the surface of Pd regions participating in hydrogenation and dehydrogenation dynamics. To gain insight into the mechanism of the observed structural and kinetic changes in the Pd environment, we performed a systematic investigation of the stability of various Pd and PdH_x structures in Au as a function of a wide range of Pd and H concentrations, by using density functional theory (DFT) calculations of Pd in model bimetallic surfaces. Using this approach, we accounted for the effects of hydrogen activation, diffusion, and absorption.

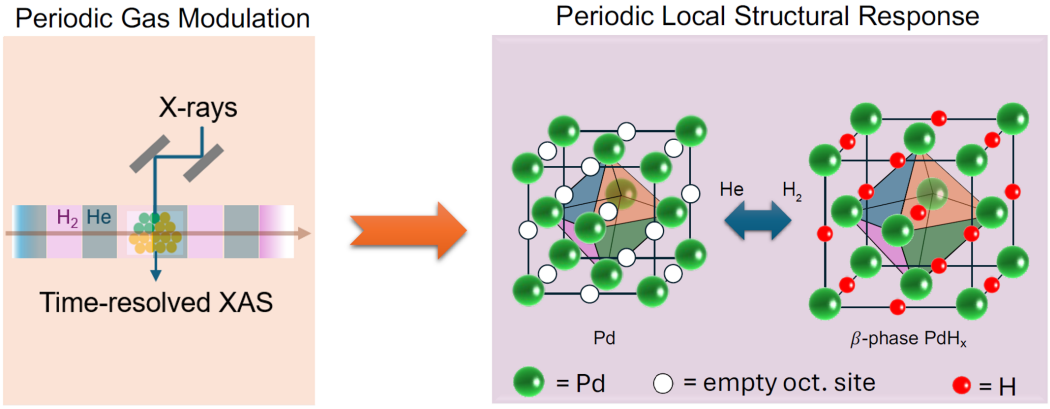

Figure 1. Schematic overview of time-resolved XAS experiments (left pane). ME-XAS experiment of Pd and 30%Pd-Au RCTs was conducted at 100 °C, while the pretreatment in He was carried out at 210°C. Transformation between the Pd and PdH_x in PdAu lattice (right pane).

2. Experimental Results and Discussion

2.1 Local structure determination of Pd and PdHx in Pd-Au RCT using steady state XAS

Prior work on PdH_x[12, 35-37] have shown that using the empirical relationship (Eq. (1)) between Pd-Pd bond length change (ΔR), determined by the steady state EXAFS measurements, and y, the H/Pd ratio of palladium hydride, the latter can be obtained for Pd in Pd nanoparticles as well as Pd-Au bimetallic nanoparticles:

$$\frac{\Delta R}{R} = 0.066y - 0.0164y^2. \quad (1)$$

Table 1 lists the best fit parameters obtained by the EXAFS analysis of spectra obtained under steady state conditions in either He or H_2 environments, indicating an increase in Pd-Pd interatomic spacing from 2.77 to 2.80 Å, yielding $\Delta R/R = 0.011$. The changes in the local coordination environment of Pd seem negligible (within the experimental error) at room temperature. We note that the ratio of Pd-Pd and Pd-Au coordination numbers (Table 1) is greater than their relative fraction (1:3) in the alloy, consistent with segregation of Pd to Pd-rich regions, as expected. Using a crude estimate of the H/Pd ratio y = 0.17 (obtained after solving Eq. (1)), two scenarios may be proposed. The first one, a homogeneous model, corresponds to H occupying, on average, 17% of all octahedral sites in all Pd regions with the nanoparticles. The second, heterogeneous, model corresponds to a fraction of regions in the H occupancy is 100%, coexisting with the metallic regions. Within the limitations of the ensemble-averaging nature of steady state XAS, we cannot resolve between these possibilities. The tie between them will be broken when ME XAS is combined with theoretical modeling (vide infra).

Table 1: Ensemble averaged EXAFS fitting results under steady state conditions at room temperature: coordination numbers, distances, their mean squared disorder values and the photoelectron energy origin corrections. The amplitude factor was obtained by the fit to Pd foil EXAFS and fixed to 0.8. Uncertainties in the last significant digits are given in parentheses. Further details are given in the SI (Section "Steady State EXAFS").

	Pre-MES (in He)	Post-MES (in He)	PdAuH: (in H_2)
$\boldsymbol{N_{PdPd}}$	3.0(1.1)	3.6(1.3)	3.2(5)
$\boldsymbol{N_{PdAu}}$	7.7(1.2)	7.6(1.4)	7.4(6)
$\boldsymbol{R_{PdPd}}$ (Å)	2.77(2)	2.77(2)	2.80(1)
$\boldsymbol{R_{PdAu}}$ (Å)	2.80(2)	2.80(1)	2.80(1)
$\boldsymbol{\sigma^2_{PdPd}}$ (Å^2)	0.008(3)	0.008(3)	0.004(1)
$\boldsymbol{\sigma^2_{PdAu}}$ (Å^2)	0.006(1)	0.006(1)	0.005(1)
ΔE_0 (eV)	3.2(6)	3.3(6)	3.2(3)

In summary, XAS analysis of spectra collected under steady state conditions shows that, from the ensemble-average perspective, the Pd-Au alloy does not undergo significant restructuring as a result of changing gas atmospheres. Furthermore, no significant change in Pd-Pd interatomic spacing is observed before and after the modulation experiment. A clear increase in Pd-Pd interatomic spacing is observed, however, when the system is exposed to H_2 at room temperature, corresponding to saturated PdH_x in the 30% Pd-Au RCT system. Therefore, modulation-excitation experiments with enhanced sensitivity to the effects of H incorporation into Pd regions may be more suitable for investigating these effects than the steady state experiments.

2.2 Time-resolved XANES and EXAFS of Pd and Pd-Au RCTs

To characterize the Pd hydride formation kinetics, we utilized the multivariate curve resolution – alternating least squares (MCR-ALS) method[38] to decompose the time-resolved spectra of the core-shell

Pd/PdH_x nanoparticle system. In this method, the variations between the spectra are first studied by principal component analysis that represents all the time-resolved spectra using a small number (*N*) of (abstract) principal components. Later, an iterative process is used to deconvolve the data matrix into the *N* spectra of unique species and their concentration profiles. The MCR-ALS analysis identified two pseudo-species in each experiment, which captured most of the signal variance. These species can be assigned to metallic Pd and the hydride PdH_x, respectively, based on the comparison of MCR-generated spectral components with reference/literature spectra for Pd and PdH_x (see Supporting Information (SI) Fig. S1). Transient processes in the beginning of H_2/He cycle were not included in the analyzed spectra by excluding the first 30 cycles for Pd and PdAu NPs. In agreement with previous reports,[39] the formation of PdH_x from monometallic Pd in H_2 flow was noticeably faster than its decomposition in He flow, as evident from Fig. 2. We estimated the characteristic time scales of the PdHx formation/decomposition as 6 and 12.2 s, respectively, by fitting a first-order exponential decay model into the corresponding signals.

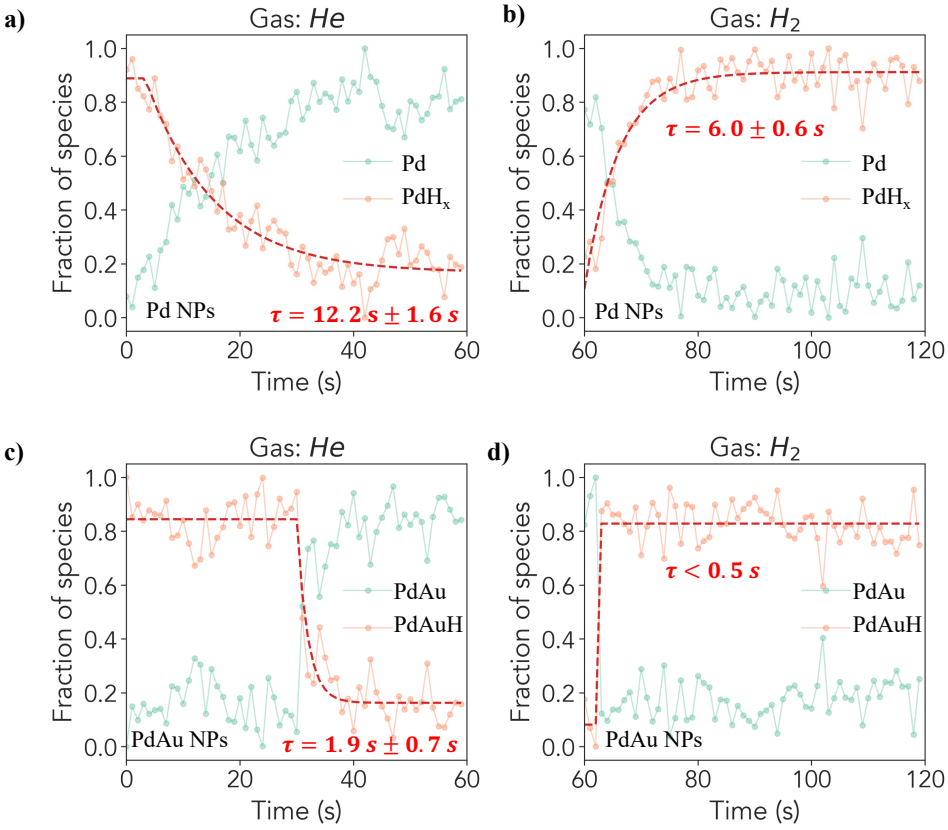

Figure 2. MCR-ALS analysis based concentration profiles for 2 species using period-averaged spectra over 30 cycles for Pd nanoparticles pretreated in He atmosphere at 210 °C. MCR-ALS analysis based concentration profiles for 2 species using period-averaged spectra over 30 cycles in PdAu NPs pretreated in He atmosphere at 1 atm. (a) and (c) correspond to He half period of 60 s, while (b) and (d) correspond to H_2 half period of 60 s. Dashed red lines show the exponential decay and rise profiles which were use to obtain time-constants of Pd hydride decomposition (Pd: 12.2 s $\pm$ 1.6 s; PdAu: 1.9 s $\pm$ 0.7 s) and formation (Pd: 6.0 s $\pm$ 0.6 s; PdAu: < 0.5 s).

As discussed above, steady-state XANES and EXAFS spectra of Pd-Au RCTs pretreated in H_2 at room temperature characterize the saturated hydrogenation state (PdAuH) of Pd-Au RCTs with an ensemble-average content of PdHx formation corresponding to a H/Pd ratio of 0.17. MCR-ALS based time-resolved XANES spectra (SI Fig. 1b) when compared with these steady state conditions, highlight that Pd-Au RCTs do not undergo complete hydrogenation and dehydrogenation between two half-cycles. Data in Figure 2 reveal important differences in the kinetics of PdHx formation/decomposition between the samples. While for monometallic Pd the decomposition of PdHx begins immediately after the flow switch from H_2 to He, a pronounced induction period of ca. 30 s is observed for bimetallic Pd-Au before PdHx begins to decompose after the switch. Additionally, it can be observed that the rates of Pd-PdHx interconversion are greater for Pd-Au than for Pd during both the formation of PdHx (characteristic time of less than 0.5 s, likely mass-transfer-limited) and its decomposition after the induction period (characteristic time of 1.9 s).

2.3 Differential XANES and EXAFS Analyses

Further insight about the reversibly forming surface and near-surface species can be obtained via demodulation of XANES and EXAFS spectra, which delineates the signal between spectators and active species.[32, 40-43] Figure 3a shows the demodulated EXAFS spectra obtained via phase sensitive detection (PSD), representing the reversible changes in the Pd-Au RCTs in phase domain. Demodulated EXAFS, in principle, encodes the average first order kinetics information which can be compared between species and/or samples, e.g. species with faster kinetics achieve maximum at higher phase angles.[41] However, in the presence of pronounced induction period and asymmetric kinetics of hydride formation

and decomposition, as seen in Fig. 2, a direct interpretation of time-domain spectra would be more helpful. Hence, a reconstruction of differential EXAFS via time domain is obtained after applying a denoising process explained in ref. [32]. In brief, the time-energy absorption coefficient 2D data matrix was processed by an iterative algorithm to remove the uncorrelated noise in time domain for each energy point. Figure 3c shows thus obtained differential EXAFS signal ($\Delta\mu = \mu(t) - \mu_{avg}$) after subtracting the time-average EXAFS signal from all individual EXAFS spectra in the full modulation period. Such subtraction isolates the signal from "spectator" species whose spectral contribution do not change reversibly during the gas modulation.

Bugaev, et al. have shown previously that spectral features in Pd K-edge XANES are also correlated with PdH_x formation.[44] Figure 3b shows a time-dependent evolution of these features as differential XANES signal with respect to the last time-step of PdAu in He half-cycle data during the modulation. A relative comparison of the spectral changes in post-MES vs pre-MES (for comparison, we also used the relative changes between the PdAuH and pre-MES as well) data and the maximum variation in the MES data shows that, approximately, up to 30% of all Pd atoms participated in Pd hydride formation/decomposition during the modulation. These denoised EXAFS data (SI Figs. S2, S4) are further analyzed by traditional EXAFS analysis (SI Figs. S3, S4). The fitting variables were the same as for the steady state analysis. All the time-dependent data were analyzed concurrently by applying the following global constraints: the same value of ΔE_0 was varied for all 120 spectra (obtained to be 4.20 ± 0.05 eV) and the Pd-Pd and Pd-Au coordination numbers were constrained to be constants as well (Fig. 3d). The H/Pd ratio was obtained to change between 8% to 11% (after applying Eq. (1) to the data shown in Fig. 3d, where the meaning of ΔR is the difference between the Pd-Pd distance in the ME EXAFS experiment and the steady state values). Hence, both differential XANES and EXAFS data show that the cyclic formation and decomposition are only partial. A closer examination of the first cycle in MES which shows only formation of Pd hydride, and no decomposition indicates fast kinetics of hydride formation (SI Fig. S5), similar to the trend shown in Figure 3b. However, the relative scale of differential XANES (Fig. 3b vs SI Fig. S5) indicates that Pd-Au undergoes near complete hydride

formation in the first half cycle of H_2 and subsequent cycles undergo only partial hydrogenation and dehydrogenation.

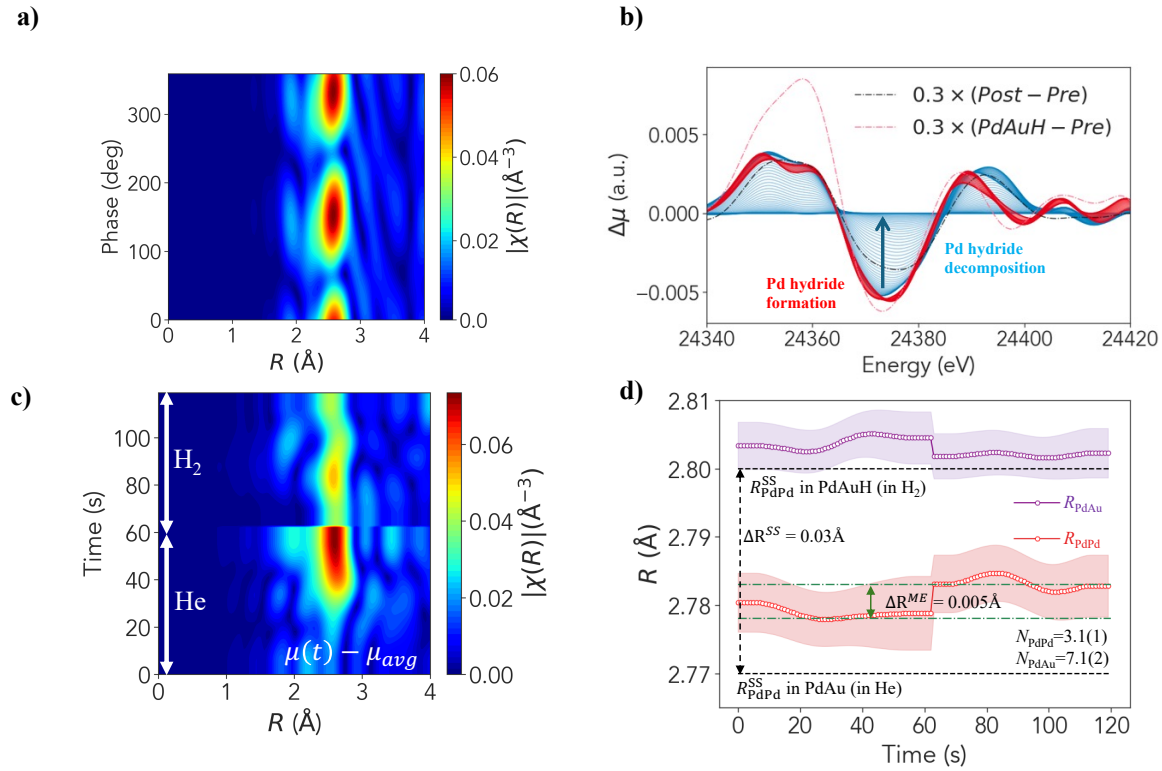

Figure 3. Phase domain (a) and denoised time domain (c) differential spectra of 30% Pd-Au RCT nanoparticles. XANES and EXAFS spectra are period-averaged over 30 cycles (C30-C60) and followed by denoising within each half pulse. b) Time-dependent differential XANES is calculated by subtracting the last spectrum in the He half-period from the period-averaged dataset. Red and blue colored spectra correspond to H_2 and He half-periods respectively. The dashed lines denote the steady-state differential XANES with respect to PdAu in He at room temperature prior to modulation: full PdAu hydride (PdAuH) at room temperature in H_2 (shown in red) and PdAu in He at room temperature after modulation (show in black). d) Time-dependent EXAFS results: interatomic spacing between Pd-Pd (shown in red) and Pd-Au (shown in purple). Black (dashes) line shows the limiting interatomic spacing, R^{SS}, under steady state conditions indicating the partial nature of hydride formation and decomposition under modulated conditions. Green (dash-dots) lines show the limits of variation of R^{ME}, the interatomic spacing between Pd-Pd, during the modulations.

Previous characterization of the Pd-Au RCT catalysts identified the presence of large Pd rich regions within the bulk Au.[7, 32, 35, 45] Our structural model arising from EXAFS analysis of time resolved ME-XAS data, also indicates that the Pd atoms are on-average coordinated with ~3 other Pd atoms. With respect to the kinetics of Pd hydride formation and decomposition, our observations indicate that, while there are similarities between the Pd-Au and Pd NPs there are also key differences. The similarity is that in both types of catalysts, Pd hydride formation occurs much faster than the decomposition. The difference is that, in Pd-Au alloys vs Pd NPs, there is a clear delay of Pd hydride decomposition in He pulse. Such delay indicates the presence of distinctly different energy barriers at the onsets of hydride formation and decomposition (Fig. 2). In addition, demodulated and differential ME-EXAFS spectra, the data (Figs. 3a, 3b and 3c) deviated from the spectral differences of the two opposite states measured under steady state conditions, with and without hydrogen. As shown in ref. [32], the demodulated data (for the O_2 and H_2 gas pulses) could be represented as the difference between the two end states (PdO and Pd metal). Modulation conditions of He and H_2 gas pulses in the current study did not lead to detectable changes of coordination environment of Pd. However, the Pd-Pd interatomic spacing changes (Fig. 3d), a proxy for PdH_x formation, showed intriguing results where partial but reversible formation and decomposition with noticeable time delays in the H_2-He pulse experiments, indicating an energy barrier at the onset of gas pulses.

We note that the interpretation of trends in the transient XAS data presented herein crucially relies on rigorous evaluation of the characteristic time scales relevant for the chemical transformations and transport phenomena within the sample. As demonstrated previously,[32] under the operating conditions in the same setup as the one used in this work, the characteristic time scale of the convective gas transport through the entire sample bed is on the order of 0.001 s, i.e., much smaller than the time scale of the changes observed in Fig. 2. We note also that XAS signal observed for monometallic Pd begins to change in response to the change of gas composition immediately after the switch in both, H_2-to-He and He-to-H_2 direction (Figs. 2a and 2b). Notably, the signal evolves at a rate that is much slower (on the order of tens of seconds) than the imposed perturbation (0.005 s) or the characteristic (plug flow reactor)

convective transport through the bed (0.001 s, *vide supra*), with PdHx formation in H_2 atmosphere being significantly faster than PdHx decomposition in He.

XAS signal observed for the bimetallic PdAu samples behaves drastically differently from the monometallic counterpart. First, the kinetics of PdHx formation/decomposition is much faster (on the order of a few seconds) for the bimetallic sample, which can be seen very clearly by comparing responses in Figs. 2b and 2d. The kinetics of PdHx formation in PdAu (Fig. 2d) is the fastest signal observed in our dataset and, as such, delineates the lower bound of the mass-transport rate at the reactor scale. In other words, even if this signal reflects the mass transport rather than chemistry, all other signals that are slower (Figs. 2a, 2b, and 2c) must definitely reflect the kinetics of chemical transformations.

The second (qualitative) difference between Pd and PdAu samples is the approximately 30 s induction period observed in Figure 2c between the start of the He half-period (H_2-to-He switch) and the start of the PdHx decomposition. In view of the aforementioned assertions regarding the rate of mass transport in the reactor, this induction period can be confidently interpreted as a purely chemical phenomenon.

In summary, experimental data and analysis results pose the following questions that, we hypothesize, can be answered in terms of the local structure and composition of Pd-Au and PdH_x species: 1) Why were the changes observed during the H_2-He modulation partial and reversible? 2) Why was there a delay in the hydrogen desorption portion of the modulation period (the hydrogen adsorption appeared to be virtually instantaneous)? 3) Why were the rates of formation and decomposition of PdH_x so different?

3. Theoretical Study

For an in-depth understanding of the stability of Pd hydride species and hydrogen diffusion pathways responsible for observed experimental barriers (for the reaction kinetics and for the presence of an induction period), we further conducted ab-initio study of various Pd hydride structures and activation mechanisms by DFT calculations. Previous work on surface and subsurface hydrogen adsorption showed that surface H_2 activation is generally exothermic and subsurface hydride formation is typically endothermic, with Pd being the only exception.[46] Weaker binding and lower diffusion barrier into the

subsurface in near-surface alloys (NSA) compared to the monometallic counterparts have been reported.[46] Hence, a stability assessment of various hydride structures under the modulated experimental conditions was carried out to identify potential stable and meta-stable candidate structures. A detailed scheme to evaluate the formation energy of various structures was shown in Fig. S6. Previous DFT studies have also suggested that the surface hydrogen diffusion barriers were quite low for all 23 transition metal surfaces that were investigated, with the barrier ranging from 0.04 to 0.28 eV.[47] A more detailed study of hydrogen diffusion pathways was conducted hereby to explain the observed hydride formation and decomposition time-scales (see Section 3.2).

3.1 Stability Assessment of Hydride Structures

A diverse range of structures with various ensembles of Pd on Au was examined using DFT calculations, sampling these structures under different hydrogen coverages and calculating their normalized formation energy (see Figs. S7 and S8). These calculations show that stable formation of hydride species under H_2 pressure reaction conditions requires extended Pd regions modelled as Pd layers on gold (Fig. S9). Here we will explore these layer models of Pd-rich regions observed in the experiments in detail.

We will first examine the hydride structures in the bilayer structure that includes two layers of Pd on two layers of Au, therefore with a total of four layers in the (3x3) periodic slab. The surface presents a (111) termination. From the initial hydrogen population where we introduced up to 9 hydrogen atoms to the 3×3 bilayer Pd slab into the surface or the subsurface layer, we observed that the surface hydrogen atoms had better stabilization effects than the subsurface hydrogen atoms. The stabilization effect was maximized with 9 surface atoms, reaching a 1:1 H-to-Pd ratio for the surface atomic layer, with all H atoms at fcc sites. Also, we were not able to find any metastable structures for the subsurface population at low hydrogen coverages (0 to 2/3 ML). Even at higher hydrogen coverage (2/3 ML to 1 ML), the subsurface-populated structures were higher in energy than the surface-populated counterparts (see Fig. S7). Therefore, the surface sites are clearly first populated and subsurface occupation only starts when the surface coverage is 1 ML.

We kept the surface layer of our 3x3 unit cell fully covered by a total of 9 hydrogen atoms and began to introduce additional hydrogen atoms in the subsurface layer. For the surface hydrogen atoms, we

considered both fcc hollow and hcp hollow sites. For the subsurface hydrogen atoms, we only took the octahedral sites (oct) into account since the octahedral hydrogen atoms were always more stable than the hydrogen atoms at the tetrahedral sites (tet) for both fcc and hcp positions of the H adlayer. Our results were in good agreement with previous work.[46, 48] Additionally, we found the vibrational entropy and zero-point energy correction pivotal in the cases where the hydrogen coverages were high, as shown in Supporting Information. This finding was also confirmed in Nazarov, et al., work.[48] Without those two factors, we inferred that it was barely likely to determine the most stable structures accurately from our calculations. Hence, the free energy calculations for structures with high hydrogen coverages included vibrational entropy and zero-point energy correction.

The normalized free energies were computed at the 4 different experimental conditions, shown in Fig. 4. At room temperature and 0.2 bar of H_2, the subsurface layer is almost fully occupied (8/9 ML coverage) and the most favorable configuration correspond to surface H atoms in the hcp position, hence in a different position compared to the case where the subsurface is vacant. Note that populating the second subsurface layer is not favorable, since octahedral sites in this layer are formed by 3 Pd and 3 Au, and the binding energy of H is unstable. At high temperature (210 °C) and low H_2 pressure (taken as 0.001 bar) no subsurface site is occupied and only surface remains completely full (H atoms in fcc sites). This suggests that modulation of the H content could be achieved by desorption of the subsurface H atoms, keeping the surface occupied. However, for the two-Pd-layer model, in the conditions of experimental modulation (T=100 °C, P varied from 0.2 bar to 0.001 bar, an estimate of the H_2 partial pressure under He flow, Fig. 4b and Fig. 4c) no modulation of the H concentration is seen, and only the surface sites are occupied. We also developed a 2D stability diagram for the bilayer model to help visualize the most stable structures under different temperature and pressure conditions (see Fig. S10).

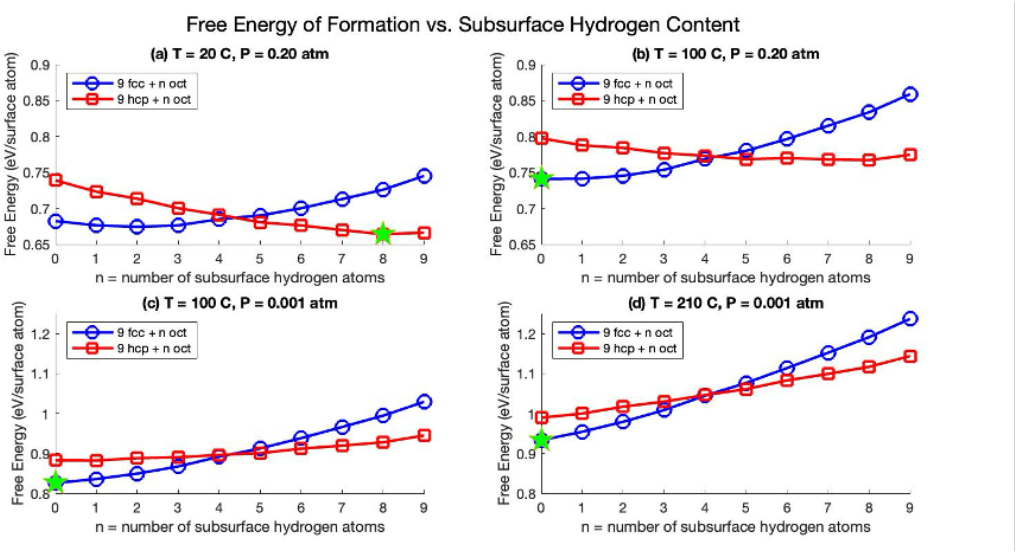

Figure 4. Free energies of formation as a function of subsurface hydrogen content for the bilayer structures under different experimental conditions from DFT calculations, a) T = 20 ºC, P(H_2) = 0.20 atm; b) T = 100 ºC, P(H_2) = 0.20 atm; c) T = 100 ºC, P(H_2) = 0.001 atm; d) T = 210 ºC, P(H_2) = 0.001 atm. All the points include the vibrational entropy and zero-point energy. In all selected conditions, the surface is completely populated with H adsorbates, that preferentially occupy the surface fcc (blue circles) or hcp sites (red circles) at resp. low or high subsurface H content. The most stable structure under each experimental condition is starred in green.

We performed similar analysis for other Pd structures, namely the Pd trilayer structure, the Pd tetralayer structure, and the pure Pd(111) structure, and the side view of each structure and its stability diagram is shown in Fig. 5. In this analysis, we did not consider the partially H covered case for each Pd layer. Only the fully vacant and the fully occupied H layers were included in the diagram. As we increased the numbers of layers of Pd, the shaded region, representing the stability region of the hydride structures, also became broadened. We also observed that all the structures would undergo modulation (as shown by the blue arrow on Fig. 5), except the bilayer structure, as discussed earlier. This could also robustly explain the experimental observations that the modulation was partial and reversible. In the modulation, the gas environment switched repeatedly between He and H_2, and hydride species exhibited very different stabilities under the two conditions. Consequently, the hydride species during the modulation changed back and forth, as the condition switched. Moreover, our DFT calculation showed that the change in the hydride species only took place in the subsurface and the surface remained fully covered

throughout the modulation. Finally, the modulation in the subsurface hydride species require significant Pd domains, which represent only a fraction of the available Pd in the system.

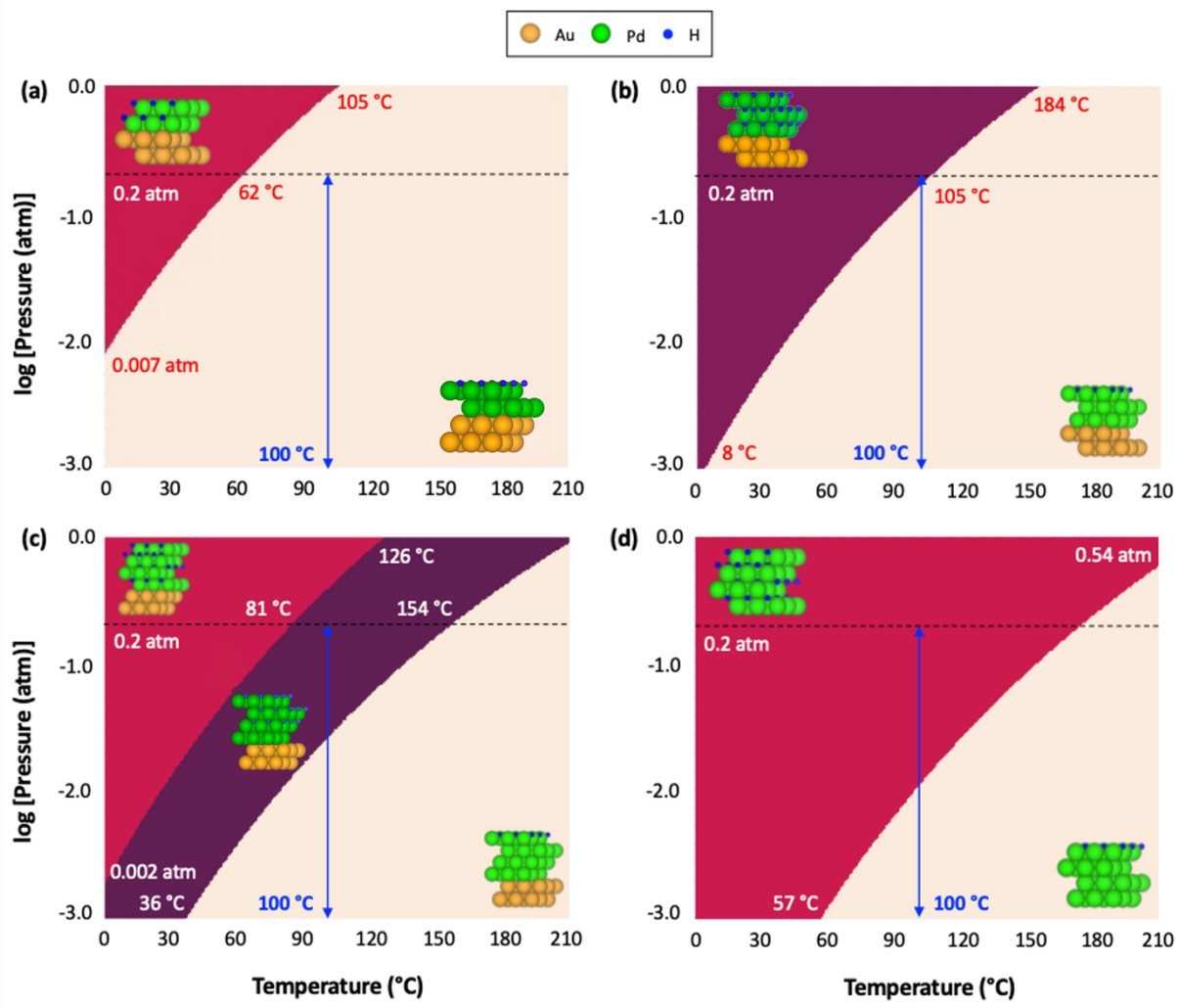

Figure 5. Stability diagram computed from *ab initio* thermodynamics for: a) Pd bilayer, b) Pd trilayer, c) Pd tetralayer, and d) pure Pd with varying surface/subsurface H concentrations. For simplicity, only the structures with the maximal number of H atoms in each layer are considered. Each layer can have a maximum of 9 H atoms in the 3 × 3 unit cell. The blue arrow indicates the experimental modulation conditions at 100 °C.

3.2 Hydride Formation and Decomposition

Removing or adding subsurface H atoms and keeping the surface site fully occupied is challenging on a mechanistic aspect since the desorption of subsurface H requires their migration via the surface, where desorption can occur. To better understand this aspect, we performed a mechanistic modelling of the

hydride formation and decomposition processes using DFT calculations. The modeling was performed on the bilayer model, and thicker models were not considered due to the high computational cost. In the decomposition process, we started with the 3x3 surface fully covered (9 hydrogen atoms in fcc positions) plus 4 H atoms in subsurface octahedral sites. We continuously removed the hydrogen atoms in the subsurface layer until only the surface was occupied (9 H in fcc sites). Two different plausible mechanisms were proposed under the He modulation conditions (T = 100 ºC and $P(H_2)$ = 0.001 atm) as shown in Fig. 6. In the pathway shown with red lines, two surface hydrogen atoms (labeled in red) are first combined, forming a surface vacancy and one H_2 adsorbate. The hydrogen molecule is then desorbed, forming a second vacancy and two subsurface hydrogen atoms migrate to the surface layer to fill up the two vacancies. The procedure was repeated to remove the two remaining subsurface H atoms. In contrast, in the pathway shown with black lines, one surface hydrogen atom (labeled in red) migrates to a nearby hcp site, opening a site for one subsurface H to migrate to the surface. This creates a metastable surface with one hydrogen atom beyond full coverage (a 9+1 H configuration) A hydrogen molecule is then formed and desorbed from the surface, and another hydrogen atom migrates to the surface to fill the new vacancy. Another two hydrogen atoms are removed in a similar fashion before reaching the structure with 9 H on the surface and no subsurface H. The black pathway has a lower overall free energy barrier (0.53 eV). The pathway of the reverse process under the H_2 modulation conditions (T = 100 ºC and $P(H_2)$ = 0.2 atm) is shown in SI Fig. S11. Furthermore, we developed pathways for hydrogen diffusion and computed the energy profile for pure Pd and AuPd alloy using different lattices (SI Figs. S12-S15). We observed that the lattice parameter could impact the energy barrier for the diffusion and that the penetration of hydrogen from the Pd layer to the Au layer was thermodynamically unfavorable.

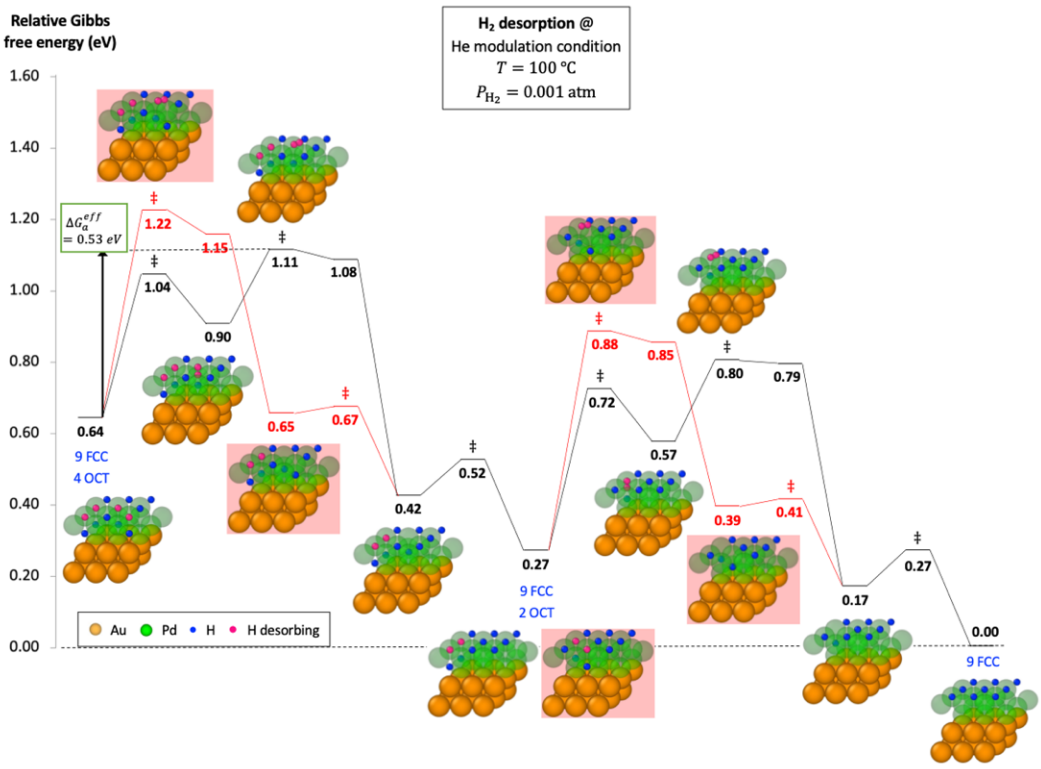

Figure 6. DFT-computed Gibbs free energy profile for the hydride decomposition process. The black and red lines represent two mechanisms under the He modulation condition, where T = 100 °C and P_{H2} = 0.001 atm.

We explain the delay for the desorption process by the necessity to remove some surface hydrogen to enable the subsurface hydrogen to migrate and desorb. As aforementioned, after the H_2 pulse in the modulation, the surface is fully covered, and there is no free channel for subsurface hydrogen content to desorb. While the thermodynamics in the He pulse allows subsurface H to desorb, this must be preceded by the desorption of more strongly bound surface H atoms, or by the formation of metastable structure with one H atom displaced, to enable a subsurface H to desorb. This creates an extra barrier for the process. The Pd-Au alloy has a larger lattice constant, resulting in a larger Pd-Pd distance for the Pd-rich regions of interest here. This results in a stronger H adsorption on the surface, resulting in a larger barrier to create the surface vacancy, and therefore a longer induction period. The delay for H desorption observed in the experiment could, therefore, be explained by a "cork" effect created by the strongly bound surface H atoms, preventing the desorption of subsurface H atoms. For the creation of

the hydride (adsorption process under H_2) H atoms at the fully occupied surface can readily penetrate in the subsurface, resulting in a lower barrier and a faster process.

4. Unifying Experimental and Theoretical Results

The insights gained by correlating the steady state and ME XAS measurements with theoretical modeling enabled us with a much more detailed picture of Pd-in-Au catalysts compared to our previous studies.[7, 35, 49] Our electron microscopy analysis utilized the high angle annular dark field (HAADF) – scanning transmission electron microscopy (STEM) imaging and elemental mapping to observe the segregation of Pd regions within the Au host (SI Fig. S16), in agreement with Refs. 32 and [35]. This observation confirms the conclusions from the steady - state EXAFS data (Fig. 7 a and b). In the current work, by combining the insights from ME-XAS experiments and theoretical modeling, we resolve more details about the Pd segregation, separating them in three groups: Pd regions near the Au surface that change dynamically between metal and hydride (we call them "active"); metallic Pd regions in the Au core and Pd hydride regions in the Au shell between the core and the surface (both of such Pd regions are "spectators" because they do not restructure in response to the H_2-He gas modulation (Fig. 7 c). In order to describe the state of the hydride in the outer region, responding to the gas modulation, we employ the observation that the difference between the ME XANES spectra between the two extremes (Fig. 3b) can be compared to the difference between the two steady-state spectra and used to quantify the relative fraction of Pd atoms that undergo restructuring which is, approximately, 0.3 (Fig. 3b), similar to the analogous scaling procedure performed previously.[32] Therefore, the changes in the average interatomic distance (Fig. 3d), which can be approximated as the weighted fraction of changes for "active" and "spectator" species, can be used to estimate the Pd-Pd distance in the Pd hydride. Hence, the interatomic spacing changes in local Pd regions (active species) should be, approximately, 1/0.3 times greater than the increase of 0.015 Å shown for the PdHx region in Fig. 3d. As a result, the $\Delta R_{active} = \langle \Delta R \rangle / x$, where x is the fraction of "active" species. Therefore, the R_{PdHx} can be estimated as 2.77 Å + 0.013/0.3 Å ≈ 2.81 Å, in a very good agreement with literature for the Pd-Pd distance with stoichiometric Pd hydride,[36] and, hence, characterizing the H occupancy in the outer region as nearly 100%.

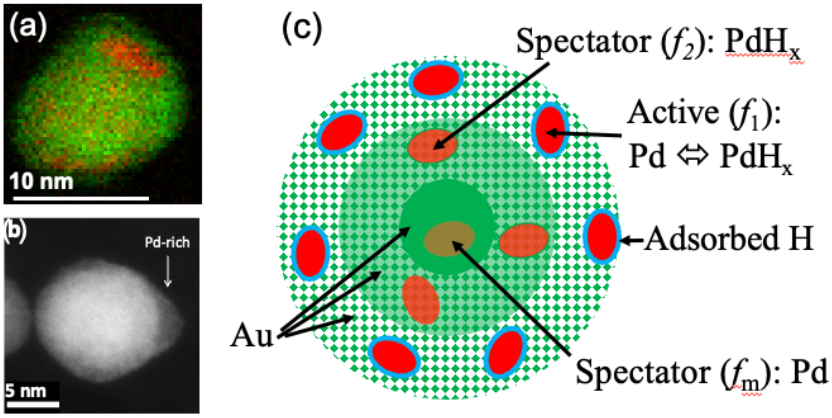

Figure 7. HAADF-STEM images of Pd distribution in previously investigated Pd-Au RCT alloys showing segregation of Pd within Au (a: Ref. [35]. Copyright (2019) Wiley. Used with permission from E. Guan et al., *New Role of Pd Hydride as a Sensor of Surface Pd Distributions in Pd-Au Catalysts*, ChemCatChem 2020, *12*, 717-721) and Ref. 32, reproduced with permission from Springer Nature (b)). Schematic of the structural changes in Pd species within the Pd-Au alloys (c, this work). Red zones represent the Pd rich regions that, in the outer shell, are active (absorb/desorb hydrogen) during H_2-He modulation.

Under the modulation excitation conditions, the changes occur between the two states of the particles (corresponding to the He and H_2 pulses) involving only outer Pd atoms with the fraction of f_1. The remaining Pd atoms, partitioned in two regions (the hydride, in the interior shell, with the fraction of f_2, and metallic, in the core, with the fraction of $f_M = 1 - f_1 - f_2$), are unaffected by the modulating atmospheres. This conclusion is based by the evidence that the Pd-Pd distance under He pulse during the ME experiment is greater than the corresponding distance under the steady state experiment (Fig. 3d), hence, some hydride phase is present in during the He pulse in the ME experiment, while under the steady state no such phase should be expected in He regime. The average Pd-Pd distances measured by EXAFS in the He pulse and in H_2 pulse are related to each other via Eqs. (2,3):

$$R_{\mathrm{He}}^{\mathrm{ME}} = (1 - f_1 - f_2)R_{\mathrm{M}} + f_2 R_{\mathrm{PdHx}} + f_1 R_{\mathrm{M}} \qquad (2)$$

$$R_{\mathrm{H_2}}^{\mathrm{ME}} = (1 - f_1 - f_2)R_{\mathrm{M}} + f_2 R_{\mathrm{PdHx}} + f_1 R_{\mathrm{PdHx}} \qquad (3)$$

Therefore,

$$f_1 = \frac{R_{H_2}^{ME} - R_{He}^{ME}}{R_{PdHx} - R_M} = \frac{\Delta R^{ME}}{R_{PdHx} - R_M} \quad (4)$$

Under the steady state conditions, the average Pd-Pd distances under He and H_2 atmospheres are related to each as follows:

$$R_{He}^{SS} = R_M$$

$$R_{H_2}^{SS} = (1 - f_1 - f_2)R_M + f_2 R_{PdHx} + f_1 R_{PdHx}$$

Therefore,

$$f_1 + f_2 = \frac{R_{H_2}^{SS} - R_{He}^{SS}}{R_{PdHx} - R_M} = \frac{\Delta R^{SS}}{R_{PdHx} - R_M} \quad (5)$$

Combining Eqs. (4) and (5) yields:

$$f_2 = \frac{\Delta R^{SS} - \Delta R^{ME}}{R_{PdHx} - R_M} \quad (6)$$

Using the results for ΔR^{SS} =0.03 Å (Fig. 3d), $\Delta R^{ME} = 0.005$ Å (Fig. 3d), $R_M = R_{He}^{SS} = 2.77$ Å (Fig. 3d), and, assuming the full H occupancy in the hydride regions, as demonstrated above, R_{PdHx}= 2.81 Å, we estimate the values for f_1, f_2 and f_M as 10%, 58% and 32%, respectively. Although this estimate is based on several approximations, the chief of them – the narrow size and compositional distributions of Pd-Au nanoparticles – have been validated in previous works.[7, 32]

As a result, by combining the steady state and ME experiments, we could resolve the heterogeneous distributions of Pd atoms in the Au nanoparticle, unavailable to either one of the experimental modes. Furthermore, theory played a critical role in arriving at this model (Fig. 7). Indeed, the presence of surface H adsorbates blocks the desorption paths of H from interior Pd regions, stabilizing them during the He pulses. Experimentally, this stabilization of H is evident via the elongation of the R_{He}^{ME} vs R_{He}^{SS} by ca. 0.01 Å (Fig. 2d).

5. Conclusions

In this work, we combined experimental techniques and theoretical tools to investigate the stability of hydride species and the kinetics of hydride formation in the AuPd alloy and pure Pd nanoparticles. In the modulation under He and H_2 gas conditions, we observed the process was partial and reversible. The DFT calculations indicated that the stability of hydride species under the two gas environments varied, and each time the gas environment changed, the hydride species changed from one to the other, making the process reversible. Moreover, only the subsurface hydrogen was modified during the modulation, and the surface remained fully covered, making the process partial.

In the experiments, we also found that for both catalysts, Pd and Pd-Au, the decomposition occurred slower than the formation process. Also, there was a noticeable delay in the decomposition process in the Pd-Au RCTs, but such delay was not observed in pure Pd. Our DFT results demonstrated an obvious cork effect that the stable hydrogen surface layer impeded the desorption of the less stable subsurface hydrogen, explaining the slower decomposition of the hydride under He modulation periods. There was no free channel for the subsurface hydrogen to desorb as the surface is fully occupied, and the desorption of subsurface hydrogen always required the removal of some surface hydrogen, which was not thermodynamically favorable. On the other hand, in the adsorption process, the surface hydrogen could easily migrate downward to the subsurface as the subsurface was completely or partially available. Also, in the alloy, the lattice was stretched by the substantial Au constituent, and the hydrogen adsorption energy was larger, making the opposite process, namely desorption, more difficult. Therefore, such delay only appeared in the alloy not in the pure Pd. Intriguingly, we noticed the rate of hydride formation in the AuPd alloy was faster than that in the pure Pd. We inferred that the hydrogen adsorption was controlled by the hydrogen diffusion. The diffusion in the pure Pd was 3-dimensional whereas it was considered 2-dimensional in the alloy as the hydrogen atoms were only enclosed within the Pd region where hydrogen adsorption was much stronger.

In summary, our integrated experimental and theoretical investigation reveals the complex interplay of stability, kinetics, and structural factors governing hydride formation and decomposition in Pd and AuPd nanoparticles, advancing our understanding of hydrogen dynamics in catalytic systems.

Experimental Methods

The samples were synthesized and characterized as explained in ref. 32. HAADF-STEM and STEM-EDX analysis was performed to study the morphology, size and metal distribution of the 30% Pd-Au RCT catalysts using a Thermofisher Spectra 300 electron microscope operated in STEM mode at 300 kV. The sample was pretreated in 20% H_2 in He at 400 ˚C for 40 min (ramp +10 ˚C/min to 400 ˚C) and cooled in He. Thereafter, it was dispersed in ethanol and drop - casted onto a carbon coated TEM grid.

The time-resolved quick-scanning X-ray absorption spectroscopy measurements at the Pd K-edge absorption were taken at the SuperXAS beamline of the Swiss Light Source, Paul Scherrer Institute, Switzerland. The setup of the ME-XAS experiments was described in details in the ref. [50]. To obtain high-quality spectra, XAS data were collected in the total-fluorescence-yield mode with a time-resolution of 0.5 s per scan, using a PIPS detector. However, processed data is used with 1s time interval. XAS in Pd foil, placed between the two ionization chambers located downstream of the reactor, was measured as reference to calibrate the energy scale. The reactor effluent was monitored during the experiments with an on-line Pfeiffer quadrupole mass-spectrometer connected to the outlet of the capillary reactor. In order to modulate the gases, two fast-acting three-way valves (Parker Series 9) synchronized with a single TTL signal actuating both simultaneously directly one flow to the reactor and another flow to the exhaust vent. Our setup imposes the switch in the inlet H_2 (or He) concentration with the nominal actuation time of 0.005 s. Using this setup a modulation excitation with period of 120 s with concentration modulation of the gas atmosphere using periodic pulse of 60 s 20% H_2 (in He) and pure He gas pulses.

ProQEXAFS[48] software was used to subtract the baseline of the pre-edge and to normalize the post-edge processing of all X-ray absorption spectra. EXAFS analysis was carried out using Fourier transform on k^2-weighted EXAFS oscillations. The curve fitting of steady state EXAFS spectra was conducted using the Artemis software of the Demeter program. The concurrent analysis of transient EXAFS with global constraints, MCR-ALS and PSD analyses were done using custom python scripts and open-source python packages: pyMCR and xraylarch.

Computational Methods

We performed DFT calculations using plane-wave basis sets and the projector augmented-wave (PAW) method[51] as implemented in the Vienna Ab Initio Simulation Package (VASP).[52] The plane-wave kinetic energy cutoff was set at 450 eV. The Methfessel-Paxton smearing scheme[53] was employed with a broadening value of 0.2 eV. All structures were optimized via ionic relaxation, with the total energy and forces converged to 10-5 eV and 0.02 eV/Å, respectively. Gas-phase H_2 was optimized in a $14 \times 15 \times 16$ Å^3 cell at the Γ-point. Lattice constants of bulk face-centered cubic Au, Pd, and Pd_1Au_3 alloy were optimized according to the third-order Birch-Murnaghan equation of state,[54, 55] using a $19 \times 19 \times 19$ and $10 \times 10 \times 10$ Monkhorst-Pack k-point grid[56] for the pure and alloy system, respectively. Unless stated otherwise, we employed the alloy lattice constant for all Pd/Au(111) slab models to reflect the global concentration of Pd in the synthesized bimetallic nanoparticles. All slab models with 4, 5, and 6 layers are spaced by 12, 14, and 16 Å of vacuum, respectively, along the direction normal to the surface to avoid spurious interactions between adjacent unit cells. We fixed the bottommost layer at bulk positions to mimic bulk properties. The Brillouin zone was sampled using a Γ-centered $5 \times 5 \times 1$, $4 \times 4 \times 1$, $3 \times 3 \times 1$, and $3 \times 3 \times 1$ k-point grid for a 3×3, 4×4, 5×5, and 6×6 unit cell of the (111) facet, respectively.

We employed the generalized gradient approximation (GGA) Perdew-Burke-Ernzerhof (PBE) exchange-correlation functional, along with the dDsC dispersion correction[57-59] to account for van der Waals interaction. PBE-dDsC provided Au and Pd lattice constants of 4.14 and 3.93 Å, within <0.1 Å of the experimental benchmark of 4.08 and 3.88 Å, respectively.[60] The optimized lattice constant of Pd_1Au_3 alloy was 4.09 Å, in good agreement with the experimental value of 4.03 Å expected from Vegard's law.[61]

Supporting Information

The Supporting Information is available free of charge on the ACS Publication website at DOI: …

MCR-ALS, EXAFS and XANES analyses of time-resolved spectra, EXAFS analysis of steady state spectra, computational details, Pd hydride stability assessment and formation process modeling, hydrogen diffusion pathways, electron microscopy analysis.

Acknowledgments

This project was primarily supported by Integrated Mesoscale Architectures for Sustainable Catalysis (IMASC), an Energy Frontier Research Center funded by the US Department of Energy, Office of Science, Office of Basic Energy Sciences, Award No. DE-SC0012573. J.S.L. used the Cannon Cluster, FAS Division of Science, Research Computing Group at Harvard University; and the National Energy Research Scientific Computing Center (NERSC), a US Department of Energy Office of Science User Facility supported under Contract No. DE-AC02-05CH11231, through allocation m3275. X.L. used the HOFFMAN2 cluster at the UCLA Institute for Digital Research and Education (IDRE).

Competing interests

The authors declare no competing interests.

References

(1) Pyle, D. S.; Gray, E. M.; Webb, C. Hydrogen storage in carbon nanostructures via spillover. *International Journal of Hydrogen Energy* **2016**, *41* (42), 19098-19113.
(2) Dong, C.; Gao, Z.; Li, Y.; Peng, M.; Wang, M.; Xu, Y.; Li, C.; Xu, M.; Deng, Y.; Qin, X. Fully exposed palladium cluster catalysts enable hydrogen production from nitrogen heterocycles. *Nature Catalysis* **2022**, *5* (6), 485-493.
(3) Kaiser, S. K.; Van Der Hoeven, J. E.; Yan, G.; Lim, K. R. G.; Ngan, H. T.; Garg, S.; Karatok, M.; Aizenberg, M.; Aizenberg, J.; Sautet, P. Identifying the optimal Pd ensemble size in dilute PdAu alloy nanomaterials for benzaldehyde hydrogenation. *ACS Catalysis* **2023**, *13* (18), 12092-12103.
(4) Zhao, X.; Chang, Y.; Chen, W.-J.; Wu, Q.; Pan, X.; Chen, K.; Weng, B. Recent Progress in Pd-Based Nanocatalysts for Selective Hydrogenation. *ACS Omega* **2022**, *7* (1), 17-31.
(5) Ball, M. R.; Rivera-Dones, K. R.; Gilcher, E. B.; Ausman, S. F.; Hullfish, C. W.; Lebrón, E. A.; Dumesic, J. A. AgPd and CuPd catalysts for selective hydrogenation of acetylene. *ACS Catalysis* **2020**, *10* (15), 8567-8581.
(6) Pei, G. X.; Liu, X. Y.; Wang, A.; Lee, A. F.; Isaacs, M. A.; Li, L.; Pan, X.; Yang, X.; Wang, X.; Tai, Z. Ag alloyed Pd single-atom catalysts for efficient selective hydrogenation of acetylene to ethylene in excess ethylene. *ACS Catalysis* **2015**, *5* (6), 3717-3725.
(7) Marcella, N.; Lim, J. S.; Plonka, A. M.; Yan, G.; Owen, C. J.; van der Hoeven, J. E. S.; Foucher, A. C.; Ngan, H. T.; Torrisi, S. B.; Marinkovic, N. S.; et al. Decoding reactive structures in dilute alloy catalysts. *Nature Communications* **2022**, *13* (1), 832.
(8) Silva, T. A.; Teixeira-Neto, É.; Borges, L. R.; Garcia, T. N.; Braga, A. H.; Rossi, L. M. From AuPd nanoparticle alloys towards core-shell motifs with enhanced alcohol oxidation activity. *ChemCatChem* **2023**, e202300180.
(9) Dimitratos, N.; Vilé, G.; Albonetti, S.; Cavani, F.; Fiorio, J.; López, N.; Rossi, L. M.; Wojcieszak, R. Strategies to improve hydrogen activation on gold catalysts. *Nature Reviews Chemistry* **2024**, *8* (3), 195-210.
(10) van der Hoeven, J. E. S.; Jelic, J.; Olthof, L. A.; Totarella, G.; van Dijk-Moes, R. J. A.; Krafft, J.-M.; Louis, C.; Studt, F.; van Blaaderen, A.; de Jongh, P. E. Unlocking synergy in bimetallic catalysts by core-shell design. *Nature Materials* **2021**, *20*, 1216-1220.

(11) Bugaev, A. L.; Guda, A. A.; Lomachenko, K. A.; Srabionyan, V. V.; Bugaev, L. A.; Soldatov, A. V.; Lamberti, C.; Dmitriev, V. P.; van Bokhoven, J. A. Temperature-and pressure-dependent hydrogen concentration in supported PdH x nanoparticles by Pd K-edge X-ray absorption spectroscopy. *The Journal of Physical Chemistry C* **2014**, *118* (19), 10416-10423.
(12) Chase, Z. A.; Fulton, J. L.; Camaioni, D. M.; Mei, D.; Balasubramanian, M.; Pham, V.-T.; Zhao, C.; Weber, R. S.; Wang, Y.; Lercher, J. A. State of supported Pd during catalysis in water. *The Journal of Physical Chemistry C* **2013**, *117* (34), 17603-17612.
(13) Haug, K.; Bürgi, T.; Trautman, T.; Ceyer, S. Distinctive reactivities of surface-bound H and bulk H for the catalytic hydrogenation of acetylene. *Journal of the American Chemical Society* **1998**, *120* (34), 8885-8886.
(14) Teschner, D.; Borsodi, J.; Wootsch, A.; Révay, Z.; Havecker, M.; Knop-Gericke, A.; Jackson, S. D.; Schlögl, R. The roles of subsurface carbon and hydrogen in palladium-catalyzed alkyne hydrogenation. *Science* **2008**, *320* (5872), 86-89.
(15) Hong, J.; Bae, J.-H.; Jo, H.; Park, H.-Y.; Lee, S.; Hong, S. J.; Chun, H.; Cho, M. K.; Kim, J.; Kim, J. Metastable hexagonal close-packed palladium hydride in liquid cell TEM. *Nature* **2022**, *603* (7902), 631-636.
(16) Morkel, M.; Rupprechter, G.; Freund, H.-J. Finite size effects on supported Pd nanoparticles: Interaction of hydrogen with CO and C2H4. *Surface Science* **2005**, *588* (1), L209-L219.
(17) Teschner, D.; Borsodi, J.; Kis, Z.; Szentmiklósi, L.; Révay, Z.; Knop-Gericke, A.; Schlögl, R.; Torres, D.; Sautet, P. Role of Hydrogen Species in Palladium-Catalyzed Alkyne Hydrogenation. *The Journal of Physical Chemistry C* **2010**, *114* (5), 2293-2299.
(18) Lewis, A. E.; Kershner, D. C.; Paglieri, S. N.; Slepicka, M. J.; Way, J. D. Pd–Pt/YSZ composite membranes for hydrogen separation from synthetic water–gas shift streams. *Journal of Membrane Science* **2013**, *437*, 257-264.
(19) Omidifar, M.; Akbar Babaluo, A. Hydrogen flux improvement through palladium and its alloy membranes: Investigating influential parameters-A review. *Fuel* **2025**, *379*, 133038.
(20) Griessen, R.; Strohfeldt, N.; Giessen, H. Thermodynamics of the hybrid interaction of hydrogen with palladium nanoparticles. *Nature Materials* **2016**, *15* (3), 311-317.
(21) Baldi, A.; Narayan, T. C.; Koh, A. L.; Dionne, J. A. In situ detection of hydrogen-induced phase transitions in individual palladium nanocrystals. *Nature Materials* **2014**, *13*, 1143-1148.
(22) Pati, S.; Jat, R. A.; Mukerjee, S. K.; Parida, S. C. Hydrogen Isotope Effect on Thermodynamic and Kinetics of Hydrogen/Deuterium Absorption–Desorption in Pd0.77Ag0.10Cu0.13 Alloy. *The Journal of Physical Chemistry C* **2015**, *119* (19), 10314-10320.
(23) Hosseini, M.; Barakat, T.; Cousin, R.; Aboukaïs, A.; Su, B.-L.; De Weireld, G.; Siffert, S. Catalytic performance of core–shell and alloy Pd–Au nanoparticles for total oxidation of VOC: The effect of metal deposition. *Applied Catalysis B: Environmental* **2012**, *111*, 218-224.
(24) Knecht, M. R.; Weir, M. G.; Frenkel, A. I.; Crooks, R. M. Structural rearrangement of bimetallic alloy PdAu nanoparticles within dendrimer templates to yield core/shell configurations. *Chemistry of materials* **2008**, *20* (3), 1019-1028.
(25) Kan, C.; Cai, W.; Li, C.; Zhang, L.; Hofmeister, H. Ultrasonic synthesis and optical properties of Au/Pd bimetallic nanoparticles in ethylene glycol. *Journal of Physics D: Applied Physics* **2003**, *36* (13), 1609.
(26) Luneau, M.; Shirman, T.; Filie, A.; Timoshenko, J.; Chen, W.; Trimpalis, A.; Flytzani-Stephanopoulos, M.; Kaxiras, E.; Frenkel, A. I.; Aizenberg, J. Dilute Pd/Au alloy nanoparticles embedded in colloid-templated porous SiO2: stable Au-based oxidation catalysts. *Chemistry of Materials* **2019**, *31* (15), 5759-5768.
(27) Merrill, N. A.; McKee, E. M.; Merino, K. C.; Drummy, L. F.; Lee, S.; Reinhart, B.; Ren, Y.; Frenkel, A. I.; Naik, R. R.; Bedford, N. M. Identifying the atomic-level effects of metal composition on the structure and catalytic activity of peptide-templated materials. *ACS Nano* **2015**, *9* (12), 11968-11979.
(28) Baber, A. E.; Tierney, H. L.; Sykes, E. C. H. Atomic-scale geometry and electronic structure of catalytically important Pd/Au alloys. *ACS Nano* **2010**, *4* (3), 1637-1645.

(29) Ricciardulli, T.; Gorthy, S.; Adams, J. S.; Thompson, C.; Karim, A. M.; Neurock, M.; Flaherty, D. W. Effect of Pd coordination and isolation on the catalytic reduction of O2 to H2O2 over PdAu bimetallic nanoparticles. *Journal of the American Chemical Society* **2021**, *143* (14), 5445-5464.
(30) Qiao, S.; Shou, H.; Xu, W.; Cao, Y.; Zhou, Y.; Wang, Z.; Wu, X.; He, Q.; Song, L. Regulating and identifying the structures of PdAu alloys with splendid oxygen reduction activity for rechargeable zinc–air batteries. *Energy & Environmental Science* **2023**, *16* (12), 5842-5851.
(31) Srinivas, S.; Vlachos, D. G. Tuning at the subnanometre scale. *Nature Catalysis* **2022**, *5* (6), 467-468.
(32) Routh, P. K.; Redekop, E.; Prodinger, S.; van der Hoeven, J. E.; Lim, K. R. G.; Aizenberg, J.; Nachtegaal, M.; Clark, A. H.; Frenkel, A. I. Restructuring dynamics of surface species in bimetallic nanoparticles probed by modulation excitation spectroscopy. *Nature Communications* **2024**, *15* (1), 6736.
(33) van der Hoeven, J. E. S.; Krämer, S.; Dussi, S.; Shirman, T.; Park, K.-C. K.; Rycroft, C. H.; Bell, D. C.; Friend, C. M.; Aizenberg, J. On the Origin of Sinter-Resistance and Catalyst Accessibility in Raspberry-Colloid-Templated Catalyst Design. *Advanced Functional Materials* **2021**, *31* (49), 2106876.
(34) Hoeven, J. E. S. v. d.; Shneidman, A. V.; Nicolas, N. J.; Aizenberg, J. Evaporation-Induced Self-Assembly of Metal Oxide Inverse Opals: From Synthesis to Applications. *Accounts of Chemical Research* **2022**, *55* (13), 1809-1820.
(35) Guan, E.; Foucher, A. C.; Marcella, N.; Shirman, T.; Luneau, M.; Head, A. R.; Verbart, D. M. A.; Aizenberg, J.; Friend, C. M.; Stacchiola, D.; et al. New Role of Pd Hydride as a Sensor of Surface Pd Distributions in Pd−Au Catalysts. *ChemCatChem* **2019**, *12* (3), 717-721.
(36) Wang, J.; Wang, Q.; Jiang, X.; Liu, Z.; Yang, W.; Frenkel, A. I. Determination of Nanoparticle Size by Measuring the Metal–Metal Bond Length: The Case of Palladium Hydride. *The Journal of Physical Chemistry C* **2015**, *119* (1), 854-861.
(37) Feenstra, R.; Griessen, R.; Groot, D. G. d. Hydrogen induced lattice expansion and effective H-H interaction in single phase PdHc. *Journal of Physics F: Metal Physics* **1986**, *16* (12), 1933.
(38) Fovanna, T.; Nachtegaal, M.; Clark, A. H.; Krocher, O.; Ferri, D. Preparation, quantification, and reaction of Pd hydrides on Pd/Al2O3 in liquid environment. *ACS Catalysis* **2023**, *13* (5), 3323-3332.
(39) Doronkin, D. E.; Wang, S.; Sharapa, D. I.; Deschner, B. J.; Sheppard, T. L.; Zimina, A.; Studt, F.; Dittmeyer, R.; Behrens, S.; Grunwaldt, J.-D. Dynamic structural changes of supported Pd, PdSn, and PdIn nanoparticles during continuous flow high pressure direct H2O2 synthesis. *Catalysis Science & Technology* **2020**, *10* (14), 4726-4742, 10.1039/D0CY00553C.
(40) Urakawa, A.; Bürgi, T.; Baiker, A. Kinetic analysis using square-wave stimulation in modulation excitation spectroscopy: Mixing property of a flow-through PM-IRRAS cell. *Chemical Physics* **2006**, *324* (2-3), 653-658.
(41) Chiarello, G. L.; Ferri, D. Modulated excitation extended X-ray absorption fine structure spectroscopy. *Phys Chem Chem Phys* **2015**, *17* (16), 10579-10591.
(42) Ferri, D.; Newton, M. A.; Nachtegaal, M. Modulation Excitation X-Ray Absorption Spectroscopy to Probe Surface Species on Heterogeneous Catalysts. *Top Catal* **2011**, *54* (16-18), 1070-1078.
(43) Marchionni, V.; Ferri, D.; Krocher, O.; Wokaun, A. Increasing the Sensitivity to Short-Lived Species in a Modulated Excitation Experiment. *Analytical Chemistry* **2017**, *89* (11), 5801-5809.
(44) Bugaev, A. L.; Guda, A. A.; Lazzarini, A.; Lomachenko, K. A.; Groppo, E.; Pellegrini, R.; Piovano, A.; Emerich, H.; Soldatov, A. V.; Bugaev, L. A.; et al. In situ formation of hydrides and carbides in palladium catalyst: When XANES is better than EXAFS and XRD. *Catalysis Today* **2017**, *283*, 119-126.
(45) Foucher, A. C.; Owen, C. J.; Shirman, T.; Aizenberg, J.; Kozinsky, B.; Stach, E. A. Atomic-Scale STEM Analysis Shows Structural Changes of Au–Pd Nanoparticles in Various Gaseous Environments. *The Journal of Physical Chemistry C* **2022,** *126* (42), 18047-18056.
(46) Greeley, J.; Mavrikakis, M. Surface and subsurface hydrogen: adsorption properties on transition metals and near-surface alloys. *The Journal of Physical Chemistry B* **2005**, *109* (8), 3460-3471.
(47) Kristinsdóttir, L.; Skúlason, E. A systematic DFT study of hydrogen diffusion on transition metal surfaces. *Surface Science* **2012**, *606* (17-18), 1400-1404.

(48) Nazarov, R.; Hickel, T.; Neugebauer, J. Ab initio study of H-vacancy interactions in fcc metals: Implications for the formation of superabundant vacancies. *Physical Review B* **2014**, *89* (14), 144108.
(49) Lee, J. D.; Miller, J. B.; Shneidman, A. V.; Sun, L.; Weaver, J. F.; Aizenberg, J.; Biener, J.; Boscoboinik, J. A.; Foucher, A. C.; Frenkel, A. I.; et al. Dilute Alloys Based on Au, Ag, or Cu for Efficient Catalysis: From Synthesis to Active Sites. *Chemical Reviews* **2022**, *122* (9), 8758-8808.
(50) Müller, O.; Nachtegaal, M.; Just, J.; Lützenkirchen-Hecht, D.; Frahm, R. Quick-EXAFS setup at the SuperXAS beamline for in situ X-ray absorption spectroscopy with 10 ms time resolution. *Journal of Synchrotron Radiation* **2016**, *23* (1), 260-266.
(51) Blöchl, P. E. Projector augmented-wave method. *Physical Review B* **1994**, *50* (24), 17953.
(52) Kresse, G. Ab initio molecular dynamics for liquid metals. *Journal of Non-Crystalline Solids* **1995**, *192*, 222-229.
(53) Methfessel, M.; Paxton, A. High-precision sampling for Brillouin-zone integration in metals. *Physical Review B* **1989**, *40* (6), 3616-3621.
(54) Birch, F. Finite elastic strain of cubic crystals. *Physical Review* **1947**, *71* (11), 809-824.
(55) Murnaghan, F. D. The compressibility of media under extreme pressures. *Proceedings of the National Academy of Sciences* **1944**, *30* (9), 244-247.
(56) Monkhorst, H. J.; Pack, J. D. Special points for Brillouin-zone integrations. *Physical Review B* **1976**, *13* (12), 5188-5192.
(57) Gautier, S.; Steinmann, S. N.; Michel, C.; Fleurat-Lessard, P.; Sautet, P. Molecular adsorption at Pt (111). How accurate are DFT functionals? *Physical Chemistry Chemical Physics* **2015**, *17* (43), 28921-28930.
(58) Steinmann, S. N.; Corminboeuf, C. A generalized-gradient approximation exchange hole model for dispersion coefficients. *The Journal of Chemical Physics* **2011**, *134* (4).
(59) Steinmann, S. N.; Corminboeuf, C. Comprehensive benchmarking of a density-dependent dispersion correction. *Journal of Chemical Theory and Computation* **2011**, *7* (11), 3567-3577.
(60) Csonka, G. I.; Perdew, J. P.; Ruzsinszky, A.; Philipsen, P. H.; Lebègue, S.; Paier, J.; Vydrov, O. A.; Ángyán, J. G. Assessing the performance of recent density functionals for bulk solids. *Physical Review B* **2009**, *79* (15), 155107.
(61) Ashcroft, N.; Denton, A. Vegard's law. *Physical Review A* **1991**, *43* (6), 3161-3164.